Preparation of Binary and Ternary Laves and μ-Phases in the Ta–Fe(–Al) System for Property Analysis at the Microscale

C. GASPER [ORCID], I.Y. GAO, F.A. BUSCH, A. ZIEMONS, D. BECKERS, H. SPRINGER, and S. KORTE-KERZEL [ORCID]

Topologically close-packed (TCP) intermetallic phases are attractive candidates for adapting the property profile of both structural and functional materials, but their mechanical behavior, in particular below their brittle-to-ductile transition, is generally still poorly understood. The systematic analysis of the underlying deformation mechanisms requires the fabrication of homogeneous samples with sufficiently high purity and large enough grain size. Here, we describe identified pathways on the example of Laves and μ-phases from the binary Ta–Fe and ternary Ta–Fe–Al systems with regard to input materials, liquid metallurgy synthesis, heat treatment, and metallographic preparation methods. Preparation routes for structural analysis by electron backscatter diffraction and mechanical analysis by nanomechanical testing, as well as the transferability of our approach to other alloy systems containing TCP phases, are outlined and discussed.

I. INTRODUCTION

INTERMETALLIC phases are ubiquitous in a multitude of metallic alloy systems, where especially their high strength up to elevated temperatures is exploited.[1,2] However, the limited understanding of their intrinsic deformation mechanisms, in particular with regard to their comparatively complex crystal structure, describable as compounds of larger A and smaller B atoms, and high brittle-to-ductile transition temperature, has so far limited their more widespread use both as bulk materials as well as precipitated compounds.[3,4] We aim to contribute to closing this gap in knowledge by focused mechanical studies of topologically close-packed (TCP) phases, which constitute a major part of the class of intermetallic compounds, including the A15, Laves (C14, C15, C36), σ-, and μ-phases.[1,4] The Laves and μ-phase in particular are closely related, as the Laves structure is a recurring part in the unit cell of the μ-phase.[5] This building block-like structure enables a systematic investigation of the TCP phases and an application of the knowledge gained to similar types of phases in other systems. For the study of their mechanical properties and deformation mechanisms, nanomechanical testing is particularly suited.[6] However, the targeted phases must be available in sufficiently large dimensions (both in bulk material size as well as in size of individual grains) to permit reliable testing. For carrying out a thorough examination of plasticity, different orientations have to be considered and the respective activated slip systems have to be determined. This requires the targeted synthesis and metallographic preparation of suitable model materials. In summary, we address the main question in this publication: How can Laves and μ-phases be synthesized and metallographically prepared to study their mechanical deformation mechanisms and properties?

For systematic studies on the dependence of deformation mechanisms and mechanical properties on crystal structure and composition, it is essential to vary these parameters independently. Therefore, synthesis and preparation routes on the example of the two closely related C14 Laves and μ-phases within the binary Ta–Fe and the ternary Ta–Fe–Al systems are presented and discussed here.[7–9] In the binary system, the Laves and μ-phase have a wide phase range of up to 13.2 and 14.5 at. pct, respectively, which allows a systematic study of the stoichiometric and off-stoichiometric compositions.[7] Furthermore, the addition of ternary elements is often of interest. Here, we included Al as substitutional element on the Fe sites,[10] which offers

C. GASPER, I.Y. GAO, F.A. BUSCH, A. ZIEMONS, D. BECKERS, and S. KORTE KERZEL are with the Institute for Physical Metallurgy and Materials Physics, RWTH Aachen University, 52074 Aachen, Germany. Contact e-mail: gasper@imm.rwth-aachen.de H. SPRINGER is with the Metallic Composite Materials, RWTH Aachen University, 52072 Aachen, Germany.
Manuscript submitted November 13, 2023; accepted March 19, 2024.

the possibility to investigate the influence of atomic size and bonding characteristics on the deformation mechanisms. The metallic radii of Ta, Fe, and Al atoms are 146, 126, and 143 pm, respectively.[11,12] The C14 Laves and the μ-phase dissolve up to about 56 and 39 at. pct Al, respectively.[8,9] For the following investigations, the Fe:Al ratio is therefore also varied and considered.

The major challenge for synthesizing these TCP phases stems from the strongly differing melting points between Ta and Fe.[7] Furthermore, not only the melting point of Al (660 °C) but also its boiling point (2470 °C) are far below the melting point of Ta (3017 °C), making it difficult to achieve the targeted compositions in the ternary Ta–Fe–Al system.[9,13]

The aforementioned close structural relationship between the Laves and μ-phase becomes clear by looking at the unit cells shown in Figure 1. The C14 Laves phase of the $MgZn_2$ type consists of alternately stacked single and triple layers, with the Fe atoms sitting on the single layer sites as well as on the center site of the triple layer.[14] When the $MgZn_2$ Laves phase structure and the Zr_4Al_3 structure[15] are stacked as building blocks in alternating order, the μ-phase is formed.[16,17] Site occupancy studies on other μ-phases[18] and atomic resolution energy-dispersive X-ray spectroscopy (EDS)[19] suggest that by adding Ta to the stoichiometric Ta_6Fe_7 composition,[16] the center atom of the triple layer may be replaced by a Ta atom, which would result in a triple layer that consists only of Ta atoms in the Ta_7Fe_6 composition.[17] The ternary Ta–Fe–Al system is investigated as well. Here, the addition of Al to the stoichiometric Ta_6Fe_7 μ-phase results in a possible replacement of the center atoms of the triple layer and the single layer atoms, depending on the amount of Al added.[20]

The two TCP phases in the Ta–Fe phase diagram, which can be seen in Figure 2 on the left, show extended homogeneity ranges at elevated temperatures.[7] In this diagram, the C14 Laves phase is described as λ-phase. It melts congruently at 1858 °C (35.0 at. pct Ta) with a total phase range from 27.7 to 40.9 at. pct Ta.[7] For the μ-phase, the phase range starts at the stoichiometric composition with 46.0 at. pct Ta to a maximum Ta content of 60.5 at. pct.[7] It is formed by the peritectic reaction $L + \lambda \rightarrow \mu$ at 1787 °C (51.6 at. pct Ta).[22] The addition of Al results in the ternary Ta–Fe–Al system, and its phase diagram is shown in Figure 2 on the right.[8] The C14 Laves and μ-phase form from the liquid at 1850 °C and 1822 °C, respectively.[8,9]

In this work, we provide an overview of how the high-melting TCP phases of the Ta–Fe(–Al) system, the C14 Laves and μ-phase, can be successfully synthesized and metallographically prepared for subsequent investigations despite their different melting points, brittleness, and hardness. To confirm the successful phase characterization and investigation, EDS and electron backscatter diffraction (EBSD) maps are presented after a detailed explanation of the individual synthesis and preparation steps. In addition, nanomechanical tests in the form of nanoindentation and micropillar compression tests are given as examples.

II. MATERIALS AND EXPERIMENTAL METHODS

In order to investigate the influence of the compositions and bonding types later, both stoichiometric and off-stoichiometric TCP phases are prepared. For the planned nanomechanical tests to determine
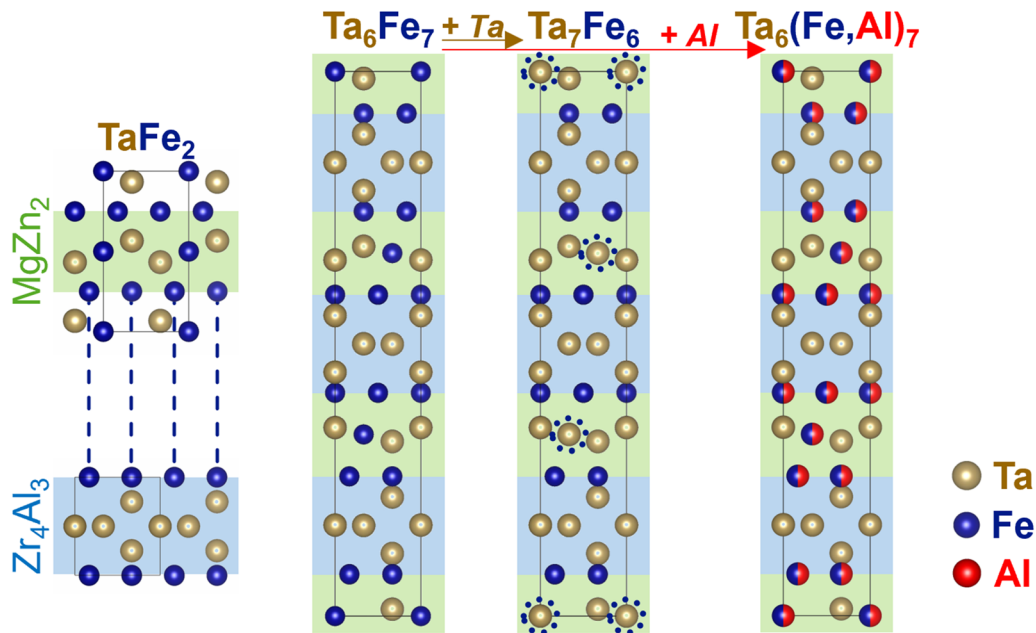

Fig. 1—Unit cells of the binary $TaFe_2$ Laves phase, the Zr_4Al_3 structure, the binary Ta_6Fe_7 and Ta_7Fe_6 μ-phase as well as the ternary $Ta_6(Fe,Al)_7$ μ-phase. The position of the Laves and Zr_4Al_3 building blocks within the μ-phase is highlighted by green and blue background, respectively. Visualization using VESTA (Color figure online).[21].
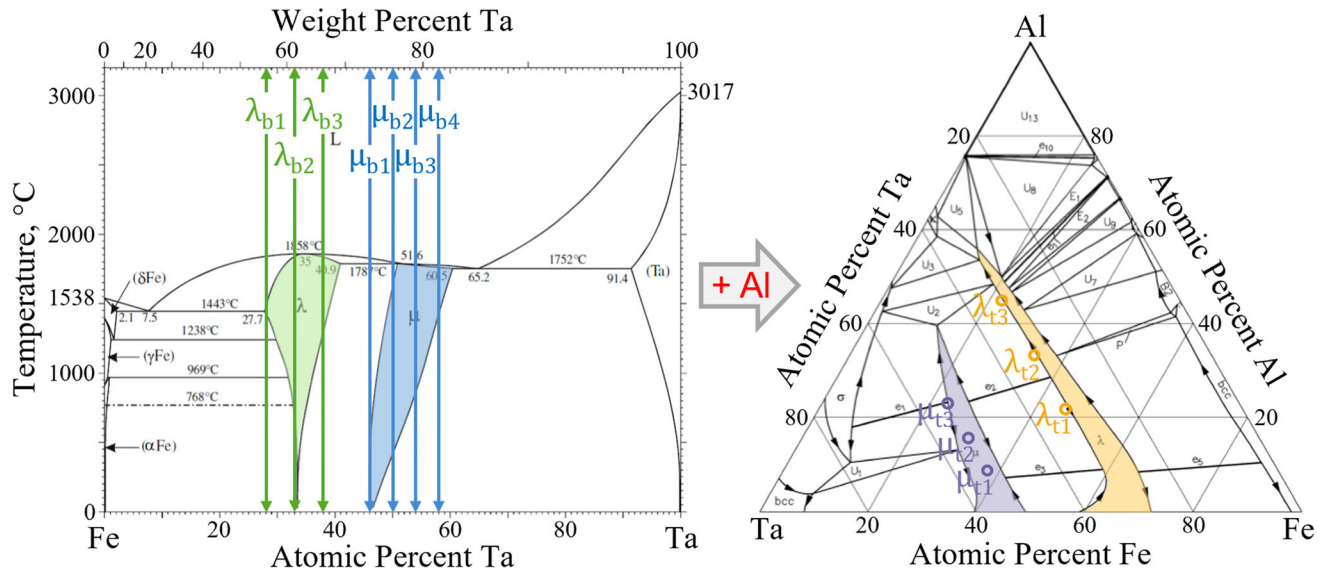
Fig. 2—Phase diagrams of the Ta–Fe (left) and Ta–Fe–Al (right) systems with the targeted compositions highlighted by arrows in the binary and circles in the ternary phase diagram. The Laves phase is denoted as λ. For the Ta–Fe–Al phase diagram, the solidus projection is chosen. Phase diagrams adapted from Refs. [7, 8] with permission from Springer.

orientation-dependent mechanical properties and their underlying mechanisms, homogeneous samples with low surface damage and sufficiently large grains are necessary to be able to carry out several tests within one grain and to investigate the orientation dependence without the influence of other phases.

The following sections are sorted according to their order in the synthesis and preparation process, see Figure 3, with both phases of both systems addressed in each step. Thus, sample preparation begins with the selection of the target sample compositions, followed by the preparation and weighing of the input materials, the sample synthesis by arc melting, the metallographic preparation (refer to Section S1.2 in the electronic supplementary material), and finally the microstructural and nanomechanical characterization with examples of the investigations enabled by the successful sample synthesis and preparation.

A. *Selection of the Target Sample Compositions*

In the binary system, the Laves phase ranges from 27.7 to 40.9 at. pct Ta and the μ-phase from 46 to 60.5 at. pct Ta, see Figure 2.[7] The nearly stoichiometric compositions were prepared for the $TaFe_2$ Laves phase with 33 at. pct Ta and the Ta_6Fe_7 μ-phase with 46 at. pct Ta. Furthermore, in the μ-phase, the Fe atoms of the triple layer can be replaced by Ta atoms, resulting in the Ta_7Fe_6 μ-phase with 54 at. pct Ta.[18,19]

In addition, off-stoichiometric compositions are relevant for a thorough characterization of both phases, as a property change is to be expected due to the altered atomic size ratio. In order to cover the entire homogeneity range of the phases as far as possible, the Ta content for the Laves phase was reduced and increased by 5 at. pct, respectively. For the Ta_6Fe_7 and Ta_7Fe_6 μ-phase, the Ta content was increased by 4 at. pct in

each case, allowing the off-stoichiometric composition between the two stoichiometric compositions as well as close to the phase boundary with a high Ta content to be represented in equal steps. This results in seven different compositions for the binary Ta–Fe system. All target compositions are indicated in Figure 2 and can be found in Table I, listing the content of the elements in both atomic and weight percentages.

In the ternary system, the Laves and μ-phase can have an Al content of up to 56 and 39 at. pct, respectively, see the solidus projection in Figure 2.[8,9] Witusiewicz *et al.*[9] calculated the liquidus and solidus projections for the Ta–Fe–Al system as well as various isothermal sections between 1700 °C and room temperature. Due to the use of an arc melter (Section II–C), where the sample is cooled to below 100 °C within a few seconds by the inert gas atmosphere and the water-cooled crucible plate, the solidus projection was chosen as a starting point for planning the sample compositions (cf. Figure 2). However, to really ensure that it is possible to prepare homogeneous Laves and μ-phase samples with the targeted stoichiometric compositions, the phase ranges of the liquidus and solidus projection as well as the isothermal section at 600 °C were superimposed, as shown in Figure 4.[8,9] In this way, the solidification process according to the ternary phase diagram is considered during the sample synthesis, whereby the process sequence is clearly defined through the use of an arc melter: the input materials are melted together, *i.e.*, they are in a liquid state and then solidify when the arc is switched off. At this point, due to the rapid cooling, which largely suppresses diffusion, it is important to be within the phase range in order to obtain the targeted phase.

Since the alloying of Al results in an additional degree of freedom that significantly increases the possibilities of sample compositions, the content of the larger Ta atoms
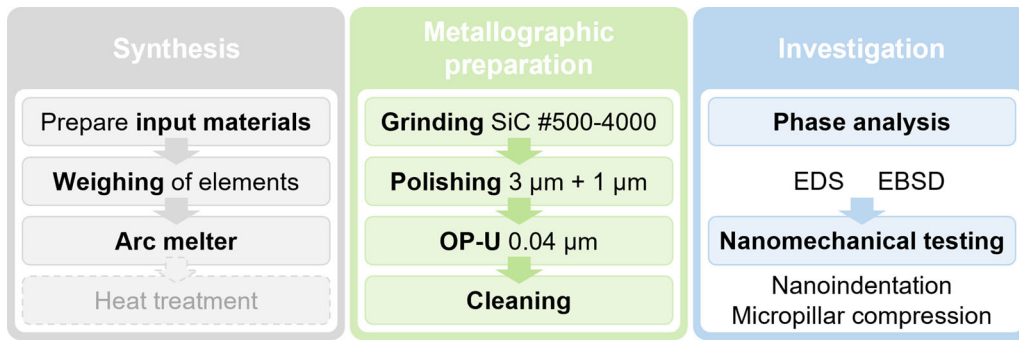
Fig. 3—Overview of the sample fabrication process: Synthesis, metallographic preparation, and investigation.

in the ternary samples was kept constant at the stoichiometry and only the relative content of Fe and Al, that more likely share the smaller sites, was varied. The prototype μ-phase with 46 at. pct Ta, where the triple layer does not only consist of Ta atoms, is not realizable in this ternary system. Therefore, the μ-phase with 54 at. pct Ta was chosen as well as the nearly stoichiometric composition of the Laves phase with 33 at. pct Ta. With the Ta content remaining constant, half of the Fe was replaced by Al as starting compound, i.e., 33.5 at. pct each of Fe and Al for the Laves phase and 23 at. pct each of Fe and Al for the μ-phase, see Table I.

For the Laves phase, the Al content can be increased by more than half the Fe content. Under the premise of varying the composition as much as possible to investigate the influence of Al on the physical properties of the system, the content of 33.5 at. pct was increased as well as decreased by 11.5 at. pct. This results in Al contents of 22 and 45 at. pct, with 33 at. pct Ta and 45 and 22 at. pct Fe, respectively (cf. Table I).

Regarding the μ-phase, Figure 4 shows the following: with a constant Ta content of 54 at. pct, a further increase of the Al content would cause the phase region to be left. Therefore, at most, half of the Fe can be replaced by Al (23 at. pct each) and the Al content was reduced accordingly in 7 at. pct steps to 16 and 9 at. pct Al. The Fe content is consequently 30 and 37 at. pct, see Table I. Altogether, this results in six different compositions for the Ta–Fe–Al system, which are marked in the superimposed phase diagrams in Figure 4. Together with the seven different compositions in the binary system, three for the Laves and four for the μ-phase, this amounts to 13 different compositions for the Ta–Fe and Ta–Fe–Al systems, which are all highlighted in the phase diagrams in Figure 2.

Furthermore, the actual compositions of the samples determined by EDS are given in Table I. The column EDS Sum given in at. pct refers to the total result of EDS area measurements including possible second phases. The EDS PoI Line column, also given in at. pct, shows the composition of the phase of interest (PoI). For this purpose, the composition of the targeted phase was determined by line measurement within the performed area measurement. Further details on the performed EDS measurements are described in Section II–E.

B. *Preparation of Input Materials and Weighing*

When selecting the input materials, a high degree of purity is of decisive importance to avoid precipitates. C impurities in particular are common for the elements used and can lead to the formation of carbides, which significantly affects the microstructure, especially the homogeneity and average grain size. Therefore, not only the amount but also the type of impurities must be considered when selecting the input materials. To demonstrate this effect, more and less pure materials and their influence on the sample synthesis were tested. The ones that led to better results in terms of sample homogeneity and grain size are written in black in Table II and are indicated together with the purity levels of the individual elements given by the manufacturers as well as the performed processing steps. They have a purity of at least 4N (99.99 pct). Tested input materials that were found to be unsuitable are listed in gray font, with the problems encountered also indicated. However, the selection of these materials was not only based on the amount and type of impurities, but also on the piece size. For the sample synthesis, a small-scale laboratory arc melter was used (Section II–C) and a total sample weight of about 2.5 to 4 g, depending on the composition, was aimed for. This requires pieces of the input materials that are as small and easy to batch as possible. In order to obtain the most accurate sample composition possible, a scale with a readability of 0.1 mg was used (Mettler ME104T). With this scale, the minimum sample weight is 16 mg and the maximum measurement deviation at the factory is 0.2 mg. To determine the conditions prevailing at the measurement location, a certified calibration weight of 5 g was weighed 10 times and a measurement uncertainty of 0.055 mg on average was calculated from these measurements.

The used Fe has a purity of 99.99 pct (included in black in Table II). It was electrolytically deposited with an increased H and O content compared to other Fe. However, this content can be reduced by remelting it.

Table I. Target Compositions of the Laves and μ-Phase Samples in the Ta–Fe(–Al) System Given in At. Pct and Wt. Pct

System	Phase	Sample	Target Composition [at.Pct]			Target Composition [wt.Pct]			EDS Sum [at.Pct]			EDS Pol Line [at.Pct]		
			Ta	Fe	Al	Ta	Fe	Al	Ta	Fe	Al	Ta	Fe	Al
Binary Ta-Fe	Laves	λ_{b1}	28	72	–	55.75	44.25	–	24.56	75.44	–	28.58	71.42	–
		λ_{b2}	33	67	–	61.48	38.52	–	30.75	69.25	–	31.70	68.30	–
		λ_{b3}	38	62	–	66.51	33.49	–	36.11	63.89	–	35.64	64.36	–
	μ	μ_{b1}	46	54	–	73.41	26.59	–	43.99	56.01	–	46.98	53.02	–
		μ_{b2}	50	50	–	76.42	23.58	–	48.38	51.62	–	48.30	51.70	–
		μ_{b3}	54	46	–	79.18	20.82	–	52.76	47.24	–	52.62	47.38	–
		μ_{b4}	58	42	–	81.73	18.27	–	57.18	42.82	–	55.53	44.47	–
Ternary Ta-Fe-Al	Laves	λ_{t1}	33	45	22	65.78	27.68	6.54	31.09	47.80	21.11	32.68	46.71	20.61
		λ_{t2}	33	33.5	33.5	68.28	21.39	10.33	31.33	36.12	32.55	32.15	33.88	33.97
		λ_{t3}	33	22	45	70.97	14.60	14.43	34.72	23.74	41.54	32.17	23.55	44.28
	μ	μ_{t1}	54	37	9	80.89	17.10	2.01	53.46	37.94	8.60	52.51	37.85	9.64
		μ_{t2}	54	30	16	82.26	14.11	3.63	53.34	31.19	15.47	53.34	30.34	16.32
		μ_{t3}	54	23	23	83.68	11.00	5.32	58.01	24.57	17.42	53.40	26.69	19.91
Ternary Ta-Fe-Al*	Laves	λ_{t2*}	30	35	35	65.19	23.47	11.34	24.34	40.76	34.90	31.98	36.73	31.29
	μ	μ_{t3*}	52	24	24	82.56	11.76	5.68	53.75	25.99	20.26	51.43	27.56	21.01

EDS sum results and EDS line measurements of the phase of interest (PoI) given in at. pct. The marking with an asterisk indicates additional ternary sample compositions used for comparison.

Another tested Fe (included in gray in Table II) appeared to have the same purity on the provided analysis data sheet, but with the C content not being analyzed. Because of difficulties with the first synthesized samples, which exhibited inhomogeneity in terms of additional unwanted phases and a small grain size, a further analysis was performed measuring three Fe pieces, resulting in an average C content of 288 ppm. For the preparation of intermetallic phases, however, C should be avoided as far as possible, as undesired reactions lead to carbide formation and fine microstructures. In case of the Ta–Fe system, Ta carbides were formed among a number of other phases. By using the remelted electrolytically deposited low-C Fe, homogeneous samples with a considerable improvement in grain size could be realized (cf. Section III–C, EBSD maps after using different input materials).

The Ta used has a purity of more than 99.99 pct and does not need to be additionally treated before use (included in black in Table II). Semi-finished Ta with a purity of 99.95 pct as a starting material was also tested, but still showed white residues from laser processing,

which are presumably oxides (included in gray in Table II). To remove these residues on the cutting edges, the semi-finished Ta was etched with 65 pct HNO_3 in water in a ratio of 1:1.5. Nevertheless, the initial purity of 99.95 pct could not be regained, as not all impurities were removable. Therefore, final synthesis was performed using the aforementioned Ta with a purity of more than 99.99 pct.

The Al used for the fabrication of the ternary samples has a purity of 99.999 pct. Since it had to be rolled for further processing, a two-step etching process was then carried out to remove the resulting contamination. For the first etching, KOH diluted in water in a ratio of 1:4 was used. The second etching step consisted of a mixture of HNO_3 and HCl in water in a ratio of 1:3:2.

Apart from the purity of the input materials, the work must of course also be clean in other regards in order to obtain homogeneous samples of the targeted compositions. To this end, all contact surfaces and objects must be cleaned before use and the tools used for mechanical comminution should be element specific.
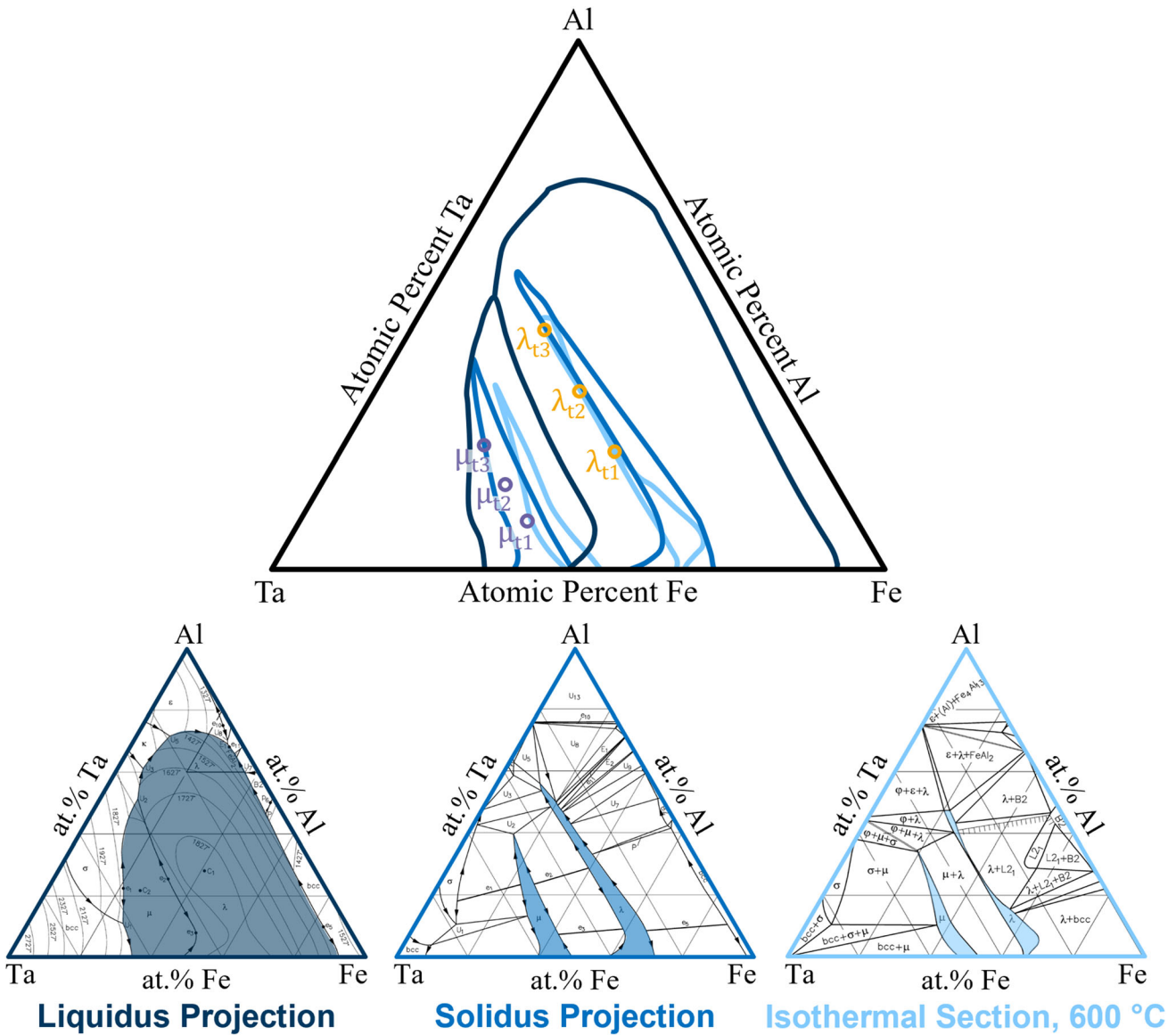
Fig. 4—Ternary Ta–Fe–Al phase diagrams with the Laves and μ-phase ranges of the liquidus and solidus projection as well as the isothermal section at 600 °C being highlighted and the targeted compositions being marked. Phase diagrams adapted from Ref. [8] with permission from Springer.

C. *Sample Synthesis Using Arc Melting*

A variety of synthesis techniques is suitable for the fabrication of Ta–Fe-based materials, ranging from powder-based solid-state sintering to large-scale induction melting. For the aims of this study, the following specific technological characteristics are most relevant: Liquid metallurgical techniques are preferable as they allow thorough homogenous intermixing of the constituting elements. The melt should ideally not be contained in refractory or graphite crucibles in order to avoid both chemical contaminations (possibly affecting phase stability regimes and deformation mechanisms) and unwanted inclusions (which could, *e.g.*, limit the grain growth aimed for here at elevated annealing temperatures). Furthermore, sufficiently high melting temperatures must be achieved in order to completely

liquify Ta (melting point of 3017 °C), and solidification should occur rapidly to avoid or at least limit segregation effects (cf. Figure 2), and thus, inhomogeneities of the sample. This is more readily achievable with smaller charge weights in the order of a few grams, which are sufficient for nanomechanical characterization methods and have the additional benefit of limiting alloy cost, although causing more effort to achieve precise chemical compositions.

These criteria can ideally be met by using a small-scale laboratory arc melter (Compact Arc Melter MAM-1, Edmund Bühler GmbH), in which sufficiently pure metals are melted on a water-cooled Cu-crucible plate under a protective gas atmosphere. In this study, charges between 2.5 and 4 g were prepared under an Ar atmosphere with a W electrode. The maximum arc current of the used arc melter is 200 A. Each sample was

Table II. Input Materials: Elements, Purity, and Processing of the Used Input Materials are Given in Black

Element	Purity	Processing/Problems
Ta	> 99.99 %	-
Fe	99.99 %	Remelting in arc melter to reduce H and O content
Al	99.999 %	Etching with KOH and HNO_3 + 3 HCl to reduce contamination after rolling
Ta	99.95 %	Semi-finished; still impurities after etching with HNO_3
Fe	99.99 %	C not analyzed

Input Materials tested in addition are indicated in gray, including the description of the problems encountered.

remelted for about 5 to 15 seconds and flipped at least four times to ensure full dissolution of Ta [cf. remaining Ta core in Figure 7(a)]. Solidification occurred in the order of 1 to 3 seconds once the arc was switched off. Al should only be added to already prepared Ta–Fe samples and subsequently remelted to avoid unnecessary overheating and evaporation.

D. *Heat Treatment and Remelting*

Heat treatment or remelting are common techniques to make inhomogeneous or fine-grained samples usable for the following investigations by homogenization, recrystallization, and/or grain growth. The heat treatment of the samples was carried out using a vacuum retort furnace, at a pressure of approximately 10^{-5} mbar and a maximum temperature of 1130 °C, measured at the sample position. Since the melting points of the TCP phases considered are above 1750 °C, *i.e.*, the heat treatment temperature is only less than two thirds of the melting temperature, long holding times of at least 500 hours were chosen. After heat treatment, the furnace was ventilated with Ar and the samples were then directly quenched in water.

Higher temperatures could be achieved using a high-frequency induction furnace (Ambrell EASYHeat 5060 LI, AMERITHERM Inc.) with a maximum power of 6 kW and a frequency of 150 to 400 kHz operated under an inert gas atmosphere, here Ar. This furnace allows both heat treatment by keeping the temperature close to the melting point and complete melting of the input materials for sample synthesis or remelting of already synthesized samples. As crucible material, Al_2O_3 as well as ZrO_2 were used, whereby ZrO_2 allows higher operating temperatures. For the Ta–Fe system, the furnace was heated to a maximum temperature of up to approximately 1900 °C at a frequency of approximately 300 kHz. Quenching of the samples is not possible with this furnace. By switching it off and increasing the Ar

gas flow, cooling to room temperature is achieved within 10 minutes.

E. *Microstructural Characterization*

To achieve a microstructure of the synthesized phases that is suitable for subsequent investigations of crystal orientation and mechanical properties, microstructure characterization, in particular of sample homogeneity, phase and texture analysis, grain size, and surface quality, is indispensable. Details on shaping of the samples and metallographic preparation are given in the supplementary material. We identified grinding as the most suitable method for shaping and long polishing times as a key ingredient for high surface quality. The samples were examined using various analytical methods: Optical microscopy (Leica LEITZ DM RM) during and after metallographic preparation, the acquisition of secondary electron (SE) and backscattered electron (BSE) images, and more in-depth analysis using EDS and EBSD (Helios NanoLab 600i from FEI Inc. equipped with Octane Super A EDS detector and Hikari XP2 EBSD detector, both EDAX; software used for EDS quantification and EBSD indexing also from EDAX).

The SE and BSE images of the different samples were taken with an accelerating voltage of 5 kV and a beam current of 0.69 nA at a working distance of 4 and 5 mm, respectively. To analyze slip traces around the indents and on the deformed micropillars, the ultra-high resolution (UHR) mode was used with a working distance of 1.8 and 4 mm, respectively, at an accelerating voltage of 5 kV and a beam current of 0.34 nA.

For EDS and EBSD measurements, the acceleration voltage was increased to 20 kV and a beam current between 2.7 and 5.5 nA was chosen. Due to the detector alignments, EDS measurements were acquired at a working distance of 4 mm and EBSD or combined maps at 10–11.5 mm working distance with a 70° pre-tilted

sample holder. The EBSD maps have a step size between 0.3 and 2.0 μm depending on the length scales of the microstructure to be analyzed. The EDS analysis was performed with a dwell time of 200 μs. For the EDS results given in Table I, area measurements with dimensions of 138 μm × 176 μm were performed. The line measurements have a length of 35 μm and 10 points each in X- and Y-direction. To evaluate the EDS measurements, the background was manually adjusted with the reference points kept constant within the phases to ensure the comparability of the different compositions. Due to the high atomic number of Ta of 73, the L line was selected, while the evaluation of Fe and Al was done based on K lines. The PeBaZAF base model was used for quantification. All EBSD maps are uncorrected. The grain orientations of the inverse pole figure (IPF) refer to the sample normal.

F. Nanomechanical Characterization

Room-temperature nanoindentation tests were performed using a load-controlled nanoindenter (iNano Nanoindenter, KLA Instruments) equipped with a diamond Berkovich indenter tip (Synton-MDP AG) and analyzed using the method defined by Oliver and Pharr.[23,24] The experiments were carried out with a maximum load of 45 mN at a strain rate of 0.2 s^{-1} resulting in a final depth between 350 and 400 nm depending on the tested sample.

For micropillar compression tests, the micropillars were prepared using a Dual-Beam FIB (Helios Nano-Lab 600i, FEI Inc.). They have an upper diameter of 2 μm, a height of around 5.25 μm, and a taper angle of approximately 3 deg. For the milling, an accelerating voltage of 30 kV was used and the beam current was decreased for each step starting from 21 nA to 80 pA. The deformation of the micropillars was done using a displacement-controlled picoindenter (Hysitron PI 89 SEM PicoIndenter, Bruker), *in situ* in an SEM (UHR SEM CLARA, TESCAN). A diamond flat punch with a diameter of 5 μm was used as indenter tip.

III. RESULTS

A. Effect of Heat Treatment on Microstructure

Inhomogeneous samples with small grain size were heat treated. Despite long holding times in the vacuum retort furnace of 504 and 672 hours at approximately 1130 °C and subsequent quenching, no significant change in the microstructure was observed. Due to the high melting points of the studied intermetallic phases of the Ta–Fe and Ta–Fe–Al systems with over 1750 °C, heat treatments accordingly need to be carried out at higher temperatures. To achieve such a temperature range, an induction furnace was used. Samples can be completely synthesized in an inert gas atmosphere or heat treated as a follow-up step after synthesis. The average grain size could, thus, be significantly increased to mm dimensions. However, inhomogeneities, like additional phases and inclusions, were not eliminated,

but intensified by reactions with and possible contaminations from the crucible material. Eventually, the more significant influence on the improvement of the microstructure was found to be the change to purer input materials, as described in Section II–B. This made subsequent heat treatment obsolete and the TCP phases with sufficient grain size could be synthesized only by using the arc melter with an adjusted synthesis route.

B. Arc Melting Procedures

1. Binary compositions

There are different ways to produce the samples from the starting materials. For example, the order in which the input materials are added, their quantity and position in the individual melting steps and also the frequency with which the sample is melted can be controlled and altered. With the aim of synthesizing a homogeneous sample of the specified composition, different process routes were tested and the produced samples were afterwards compared with each other. In the binary system, the following production process, shown in Figure 5 on the left, proved to be the most successful: First, the Fe is remelted three times, as explained in Section II–B. Between the melting steps, the sample bead is always turned over, since its bottom side solidifies faster due to the water-cooled Cu-crucible plate. Without turning, it is possible that the bead was not liquified entirely, resulting in an inhomogeneous sample with insufficiently dissolved starting material. Then the weighed Ta pieces are placed next to the resulting Fe bead. The metal with the higher melting point, in this case the Ta, is melted, which drags the lower-melting Fe into the Ta melt. It is important to avoid melting the Ta pieces together first, because due to its high melting point and the limited power of the arc melter, remelting larger Ta beads can be not completely possible. As the Ta content increases, melting also becomes more difficult, which is why the sample size must be adapted to the available furnace. Especially for the μ-phase with its high Ta content of at least 46 at. pct, a homogeneous composition could not always be achieved. Often the samples still had a Ta core even after repeated remelting, see Section III–B–4.

2. Ternary compositions

The optimized synthesis route for the ternary Laves and μ-phase is also illustrated in Figure 5 on the right. The Fe is remelted three times, and between the melting steps, the bead is turned over as in the binary system. Ta is added to the Fe bead and melted again two times with the melting process starting from the Ta side. In Figure 5, the Ta is marked with a small (1), meaning that this is only the first part of the total Ta amount added. This subdivision of the Ta content results from the additional alloying of the third element, the Al. As already discussed, Ta and Al in particular differ in their melting points, which is why they should not be melted together directly. By melting the Ta and Fe together first, as in the binary system, the melting point can be lowered before the Al is added. However, since the Fe in the ternary system is to be partially replaced by Al, the
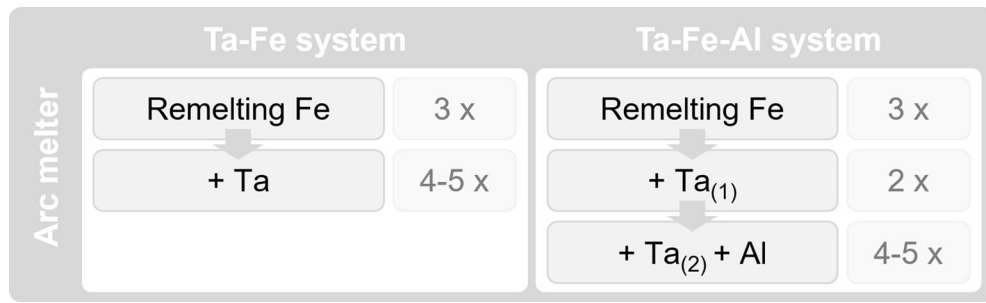
Fig. 5—Arc melter process for synthesizing Laves and μ-phase samples of the binary Ta–Fe (left) and the ternary Ta–Fe–Al (right) systems. The order of addition of the input materials and the melting times are indicated.
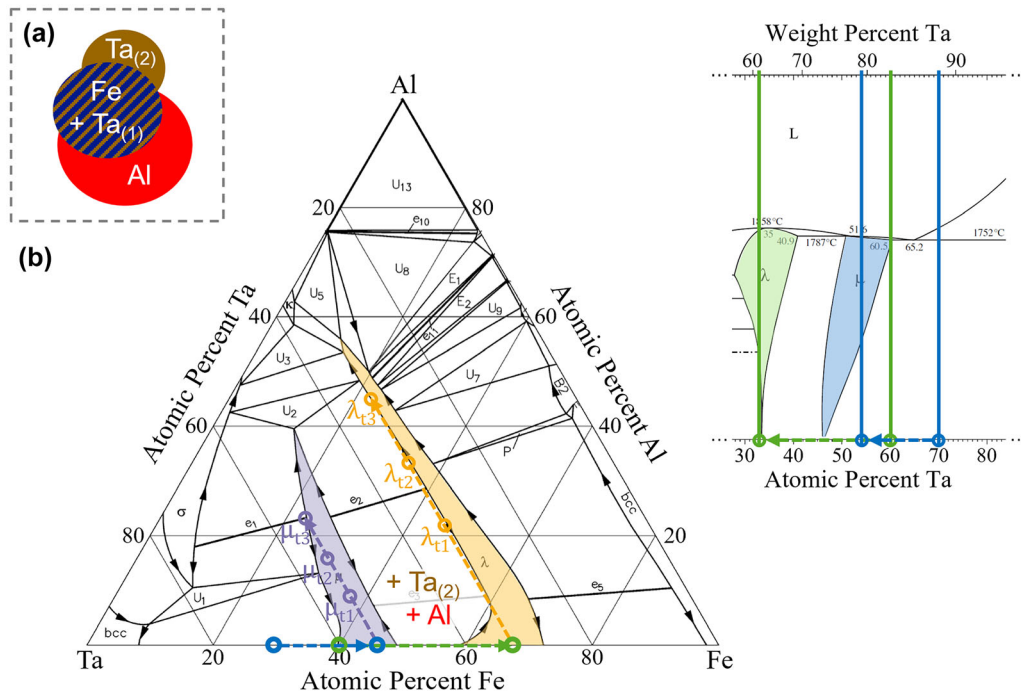

Fig. 6—(a) Typical arrangement of the input materials in the arc melter; (b) schematic illustration of the compositional pathways of the melt in the ternary phase diagram after reducing the Ta content in the first synthesis step, as also marked in the section of the binary phase diagram, taking the ternary Laves and μ-phase samples with the highest Al content (samples λ_{t3} and μ_{t3}) as examples. The final compositions of all ternary samples are given for a complete overview. Phase diagrams adapted from Refs. [7, 8] with permission from Springer.

Ta:Fe ratio is not correct in this first melting step. Instead, a composition far outside the Laves or μ-phase field is present if the full Ta and Fe content without the Al is used. This is indicated in Figure 6(b) by the green and blue circles positioned outside the respective phase fields (taking the samples with the highest final Al content as examples). Starting with the final Ta and Fe contents of the alloys therefore results in two particular scenarios that should be avoided: the formation of additional phases that complicate the preparation of the intended homogeneous phase and the presence of a large amount of Ta that is difficult to remelt completely after being melted to a sample bead. Both lead to a deviation from the target composition. In order to prevent this, the extended synthesis route in Figure 5 has to be employed.

We illustrate this route with reference to the binary and ternary phase diagrams in Figure 6 in terms of the anticipated evolution of the composition for the Laves and μ-phase samples with the highest Al content, *i.e.*, for sample λ_{t3} and sample μ_{t3} (cf. Table I). By melting the entire weighed-in Ta and Fe quantities for the two samples, the Ta content would be about 60 at. pct for the Laves and about 70 at. pct for the μ-phase, and thus, far outside the phase range of the binary phases, as highlighted in green and blue, respectively, in Figure 6(b). For the other ternary Laves and μ-phase samples with a lower Al content, the shifts outside the phase range are correspondingly lower. By subdividing the Ta content, however, it is possible to first produce the binary phase, to which the second part of the Ta and the Al are then added in the next step, maintaining a

constant ratio of A to B atoms throughout. To achieve this, the two input materials are arranged around the binary sample in such a way that they are not in direct contact with each other, as shown schematically in Figure 6(a). Melting then ideally takes place from the side of the binary sample bead, drawing the additional Ta and Al into the melt simultaneously. However, depending on the power of the arc melter used, it may be necessary to preheat larger quantities of Ta due to its high melting point. The resulting sample bead is melted at least four times and turned over in-between the melting steps (cf. Figure 5).

When testing the optimized synthesis route, it became apparent that a precise weighing-in for the first synthesis step (initial Ta + Fe) is particularly important for the μ-phase with a high Al content. For the ternary Laves phases, on the other hand, synthesis was also possible with deviations from the phase field in the first step, particularly in case of the lower Al contents. In this case it was sufficient to ensure that no homogeneous binary sample was initially produced from the entire Ta amount, but following the improved synthesis route led more reliably to a successful synthesis.

Besides the presented route for synthesizing the Laves and μ-phase of the ternary Ta–Fe–Al system by first melting Ta and Fe together as in the binary system and then adding Al after lowering the melting point, another possibility is to first add the Al to the Fe. Thereby the melting point is increased, and Ta can be added. Both process routes were tested several times and showed similar results regarding the homogeneity of the samples as well as the grain size. Based on these findings, the production *via* the binary Ta–Fe system was chosen to ensure comparability of binary and ternary samples and allow easier transfer of insights on binary sample synthesis to the ternary system.

3. *Dealing with brittleness*
Due to the high residual stresses in the samples of the intermetallic phases, the beads often break or even shatter into many small pieces during remelting or cooling. To prevent this, it is advisable to heat the Cu-crucible plate slightly for 10 to 20 seconds, and thus, indirectly also the sample before it is melted. An arc current of around 30 pct of the nominal power of the used arc melter has proven to be sufficient for this purpose. During solidification, samples have sometimes also been observed to break into two or three pieces, but splitting into many smaller pieces was rather uncommon. It is possible to heat the crucible plate, and thus, indirectly also the sample a little longer, although this affects the quenching result. For the samples presented here, the crucible plate was slightly heated before the sample bead was melted again and also for a few seconds during solidification. By that, the loss of material due to splintering of the sample could be minimized, leading to more homogeneous samples without noticeably affecting the microstructure.

4. *Dealing with very high melting points*
In the Ta–Fe–Al system, the melting point of Ta is about 2350 °C higher than the melting point of Al and around 550 °C above its boiling point. In addition to the challenge of phase formation outlined above and used to identify an adapted synthesis path, two further challenges exist: the ability to melt the very high-melting Ta and to achieve this without losing Al due to boiling by minimizing the power and time used to melt Ta.

In a small-scale laboratory arc melter, the first is the more difficult challenge to address. If the Ta is melted incompletely, a Ta core remains, as shown in Figure 7. A ternary μ-phase sample with 52 at. pct Ta and 24 at. pct Fe and Al each was planned to be prepared. The fact that at least the sample core has a different phase than the rest of the sample is visible to the bare eye (Figure 7(a)). In Figures 7(b), (d), and (e) the element distribution of Ta, Fe and Al from EDS is given, with an imbalance clearly visible. These maps confirm that the phase in the sample core consists almost entirely of Ta, while Fe and Al are found nearly exclusively in the outer phase. The rest of the sample has a correspondingly lower Ta content than expected and formation of a Ta core must therefore be avoided to achieve the targeted compositions and phases.

The Ta core of the ternary μ-phase sample shown in Figure 7 was formed due to insufficient power of the arc melter, with a limited capacity of 6 kW. Even at full power, this is apparently not sufficient for preparing 4 g samples of the ternary μ-phase that has a high Ta content of over 80 wt. pct. By reducing the sample weight to 2.5 or 3 g, a higher temperature can be reached at the same power, which is sufficient to melt the pure Ta also inside the sample.

The other challenge explained above that while melting the Ta completely, the minimization of Al loss must be considered at the same time, is exemplified by the ternary Laves phase. If the energy and time of the synthesis process are kept to a minimum to avoid Al loss, even the Ta amount of the Laves phase that is much smaller compared to that of the μ-phase, cannot be completely melted and a Ta core remains. As a result, the Ta content of the remaining sample deviates from the target composition. The effect of dissolving a Ta core and simultaneously deviating the alloy content by only a few percent is obvious at higher spatial resolution, shown for the ternary Laves phase, where the Ta content was increased from 30 at. pct including a Ta core of about 1.5 mm diameter (sample λ_{t2*}) to 33 at. pct without core (sample λ_{t2}, cf. Section III–C and the EBSD maps in Figure 8 and 9). Both compositions lie close to the boundary of the phase field of the Laves phase. Due to the remaining Ta core in sample λ_{t2*} and the resulting additional reduction of the Ta content in the rest of the sample, a much higher volume fraction of the residual second phase can be observed compared to sample λ_{t2}.
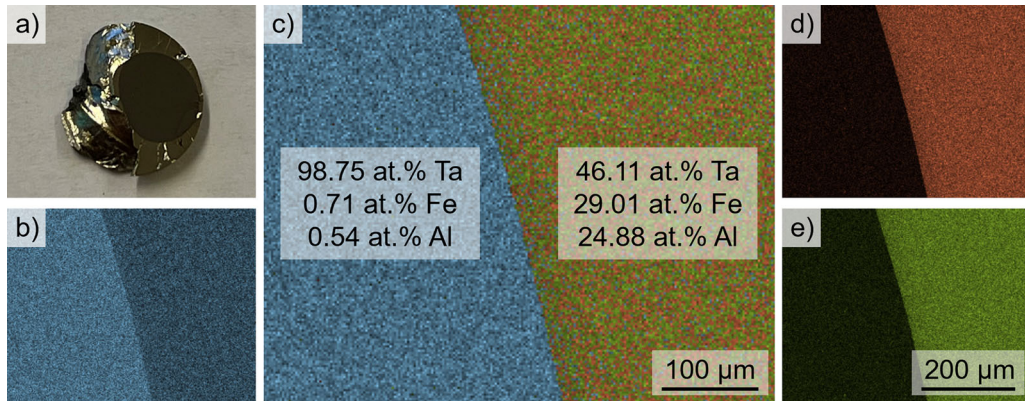
Fig. 7—EDS map of the ternary μ-phase with a targeted composition of 52 at. pct Ta and 24 at. pct Fe and Al each; (*a*) inhomogeneous sample with at least two phases; (*b*) element distribution of Ta; (*c*) EDS analysis of the phase boundary region indicating the measured compositions of the two phases; (*d*) element distribution of Fe; (*e*) element distribution of Al. The scale bar in image (*e*) also applies to image (*b*) and (*d*).

C. *Impact of Starting Material Purity and Improved Synthesis Process*

The purity of the starting materials proved to have a major impact on the phase and grain formation. A comparison of EBSD maps is shown in Figure 8 and 9 for the standard route that is without any remelting, ordering, or dividing of the input materials, and the improved synthesis route, as described in Section III–B–1 for the binary and in Section III–B–2 for the ternary compositions, in addition to using higher-purity input materials. In Figure 8, the improvement for two Laves and μ-phase samples of the binary Ta–Fe system is illustrated as a combination of IPF and image quality (IQ) maps. The Laves phase sample in (a) with a Ta content of 33 at. pct shows slight inhomogeneities as well as a relatively fine grain structure. By changing the input materials towards the untreated Ta with higher purity and the remelted Fe with lower C content, and following the improved synthesis route for binary compositions described in Section III–B–1, homogeneous samples with much larger grains could be synthesized. The resulting Laves phase sample λ_{b2} is shown in image (b).

The same applies to the μ-phase samples, where the improvement is even more pronounced. Here, the grain size could be increased from a few μm, as seen for the first μ-phase sample with 53 at. pct Ta in image (c), up to mm dimensions for the μ-phase sample μ_{b3} with 54 at. pct Ta shown in (d).

Microstructural improvements were also achieved for the TCP phase synthesis of the ternary Ta–Fe–Al system, as shown in Figure 9. Since the binary samples were prepared first, the gained knowledge could be used directly for the synthesis of the ternary Laves and μ-phase samples. However, the addition of the Al also creates new challenges regarding the sample synthesis, *e.g.*, because of the different melting points of the input materials. In the ternary case, all samples were synthesized with the remelted low-C Fe. The EBSD maps (Figure 9) reveal the effect of changing the Ta input material towards higher purity and selecting the improved synthesis route for ternary compositions, as described in Section III–B–2.

The ternary Laves phase sample λ_{t2*} with 30 at. pct Ta in Figure 9(a) already has a relatively large grain size, but also shows the presence of a second phase, which could be determined by EBSD as B2 FeAl with a cubic crystal structure. It formed due to the already low Ta content and an additionally remaining small but almost pure Ta core. Consequently, the formed Laves phase also deviates from the target composition (cf. EDS measurement results of sample λ_{t2*} in Table I). This issue of insufficient melting after the addition of a further element with a much lower melting point, has already been addressed in more detail in Section III–B–4. By changing the Ta input material, selecting the better synthesis route for ternary compositions as explained in Section III–B–2, and increasing the Ta content by 3 at. pct, the proportion of the second phase could be significantly decreased. The improved microstructure of the ternary Laves phase sample λ_{t2} with 33 at. pct Ta can be seen in Figure 9(b).

D. *Evaluation of the Metallographic Preparation*

The metallographic preparation of the TCP phases in the Ta–Fe(–Al) system, as described in the supplementary material (Section S1.2), proved to be suitable for the following investigations. Due to the long polishing times, the sample surface is processed without strong mechanical impact. In this way, breakouts due to the brittleness of the sample material, which lead to scratching of the surface, can be minimized. One examination method that requires careful sample preparation are EBSD measurements. In order to obtain high-quality maps, the recorded Kikuchi patterns must also have a high image quality, which allows a clear recognition and determination of the band structures. This is for the investigated TCP phases even more crucial due to the close crystallographic relationship between the two considered phases, with the Laves phase also contained as a building block in the μ-phase.
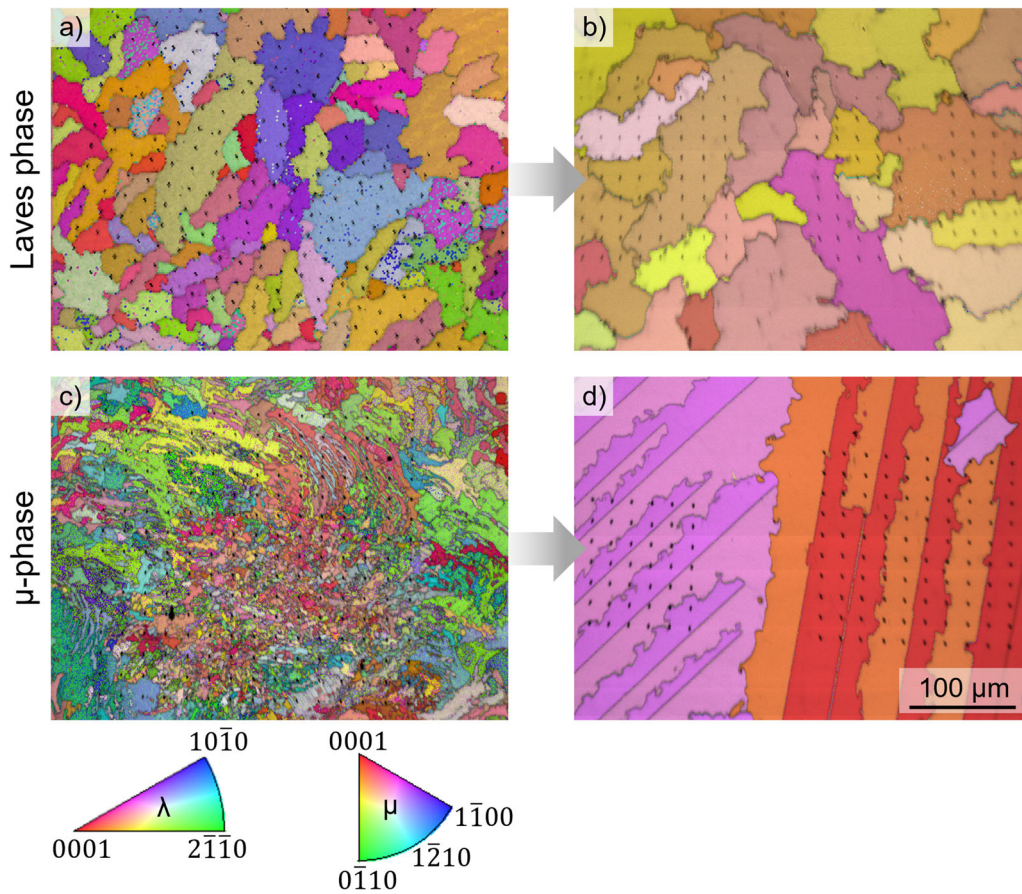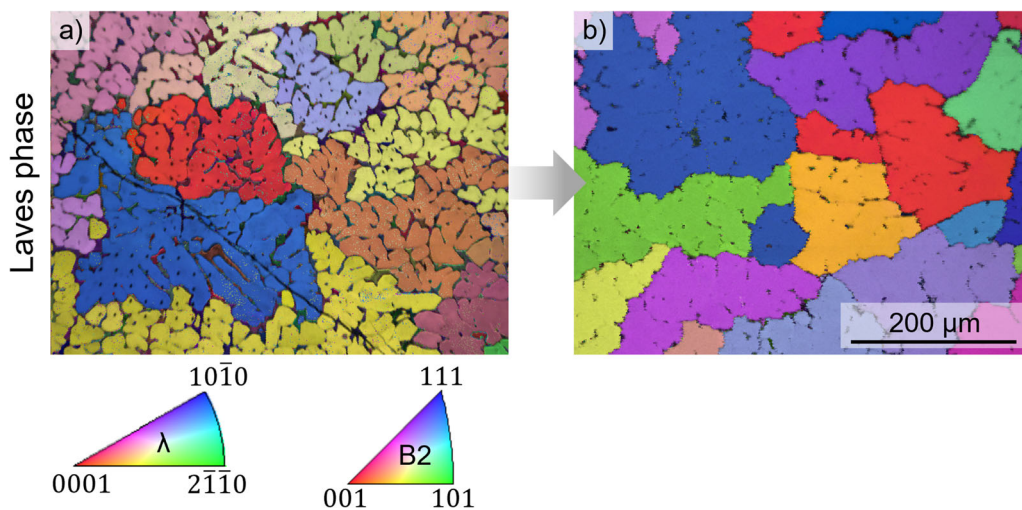
Fig. 8—EBSD maps (IPF + IQ) of binary Laves and μ-phase samples given with the corresponding IPF legends; (*a*) Laves phase sample with 33 at. pct Ta, prepared with the semi-finished Ta and C-containing Fe; (*b*) Laves phase sample λ_{b2} with 33 at. pct Ta, prepared with the purer Ta and low-C Fe using the improved synthesis route for binary compositions; (*c*) μ-phase sample with 53 at. pct Ta, prepared with the semi-finished Ta and C-containing Fe; (*d*) μ-phase sample μ_{b3} with 54 at. pct Ta, prepared with the purer Ta and low-C Fe using the improved synthesis route for binary compositions. The scale bar applies to all images.

Fig. 9—EBSD maps (IPF + IQ) of ternary Laves phase samples given with the corresponding IPF legends; (*a*) ternary Laves phase sample λ_{t2*} with 30 at. pct Ta and 35 at. pct Fe and Al each and a remaining Ta core of about 1.5 mm diameter, prepared with the semi-finished Ta; (*b*) Laves phase sample λ_{t2} with 33 at. pct Ta and 33.5 at. pct Fe and Al each, prepared with the purer Ta using the improved synthesis route for ternary compositions. The scale bar applies to both images.
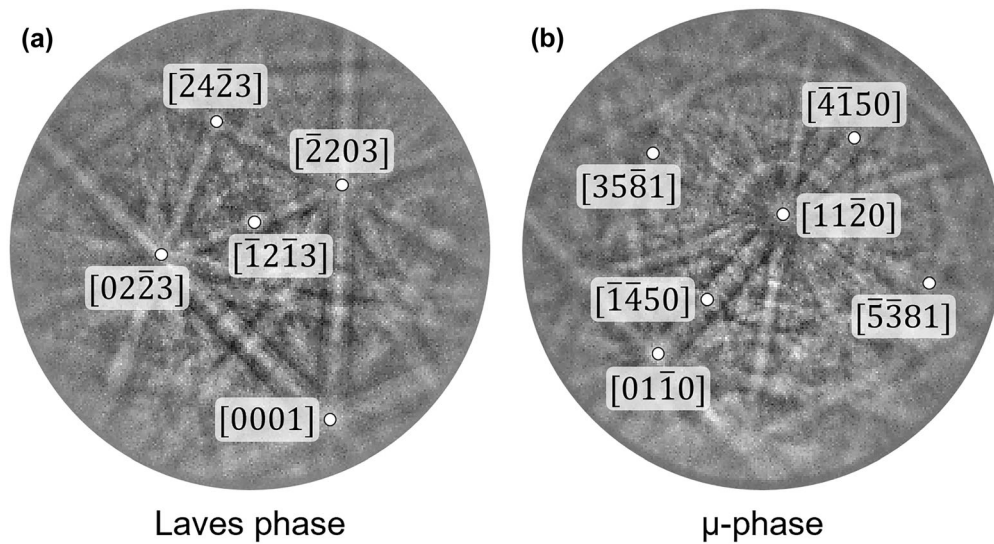
(a) Laves phase — indexed zone axes: $[\bar{2}4\bar{2}3]$, $[\bar{2}203]$, $[\bar{1}2\bar{1}3]$, $[02\bar{2}3]$, $[0001]$

(b) μ-phase — indexed zone axes: $[\bar{4}\bar{1}50]$, $[35\bar{8}1]$, $[11\bar{2}0]$, $[\bar{1}450]$, $[\bar{5}\bar{3}81]$, $[01\bar{1}0]$

Fig. 10—Kikuchi pattern with indexed zone axes of the (*a*) binary Laves phase and (*b*) binary μ-phase.

Examples of captured patterns with indexed zone axes are shown in Figure 10. The pattern of the binary Laves phase is given in (a) and the one of the binary μ-phase in (b).

E. *Phase Analysis by EBSD and EDS*

By combining EBSD with EDS on metallographically well-prepared surfaces, the microstructural analysis can be complemented by an analysis of crystal structure and orientation as well as local chemistry, and thus, enable a clear phase distinction. The distinction between crystallographically very different phases, *e.g.*, the hexagonal Laves phase and any precipitated cubic B2 FeAl phase, is possible without difficulty using EBSD alone. In case of the two intermetallic phases under consideration, namely the Laves and μ-phase, a distinction based on the crystal structure is, however, much more difficult, due to the close relationship of these structures, with the Laves phase being a building block of the μ-phase. For this reason, the combination of EBSD with EDS is useful, since the two TCP phases differ significantly in their compositions. Figure 11 shows such a combined measurement of the binary μ-phase sample μ_{b1} that has a targeted composition of 46 at. pct Ta. The measurement could confirm the presence of the Laves phase as a second phase. In image (a) the IPF of the Laves and μ-phase is given. For a better differentiation of these phases, the IPFs of only the μ-phase and only the Laves phase are shown in image (b) and (c), respectively. In addition, the color-coded phase map can be seen in image (d), with the μ-phase highlighted in red and the Laves phase in green. These EBSD maps agree with the EDS results, which, as seen in (e), show a higher Ta concentration in the matrix and a correspondingly higher Fe concentration, given in (f), in the second phase identified as Laves phase.

In addition, it is also of decisive importance that the phase files are as accurate as possible in order to distinguish the intermetallic phases. After selecting the reflectors listed in Table III together with a good pattern quality, it is possible to distinguish the Laves and μ-phase by EBSD alone.

F. *Overview of all Prepared Samples*

For all samples listed in the upper part of Table I, optical microscopy images were taken, which can be seen in Figure 12. In images (a–c) of the first row, the binary Laves phases λ_{b1}, λ_{b2}, and λ_{b3} are shown, which were weighed in at Ta fractions of 28, 33, and 38 at. pct, respectively. The samples of the binary μ-phases μ_{b1}, μ_{b2}, μ_{b3}, and μ_{b4} can be seen in images (d–g) in the row below. They were weighed in at 46, 50, 54, and 58 at. pct Ta, respectively. Both the Laves and μ-phase samples are sorted by increasing Ta content. In the next two rows, the samples of the ternary Ta–Fe–Al system are given. Samples λ_{t1}, λ_{t2}, and λ_{t3} of the ternary Laves phase are shown in images (h–j). They are sorted by increasing Al content of 22, 33.5, and 45 at. pct, respectively, while the Ta content remains constant at 33 at. pct. The ternary μ-phase samples are also sorted by increasing Al content at a constant Ta content of 54 at. pct. Images (k–m) show the samples μ_{t1}, μ_{t2}, and μ_{t3} with targeted Al contents of 9, 16, and 23 at. pct, respectively. The undeclared percentage of the sample compositions is always Fe.

Based on these images, which depict an area of the samples of several 100 μm side lengths, it can be seen that the samples mostly have a consistent microstructure over their entire surface and are not divided into several different regions.
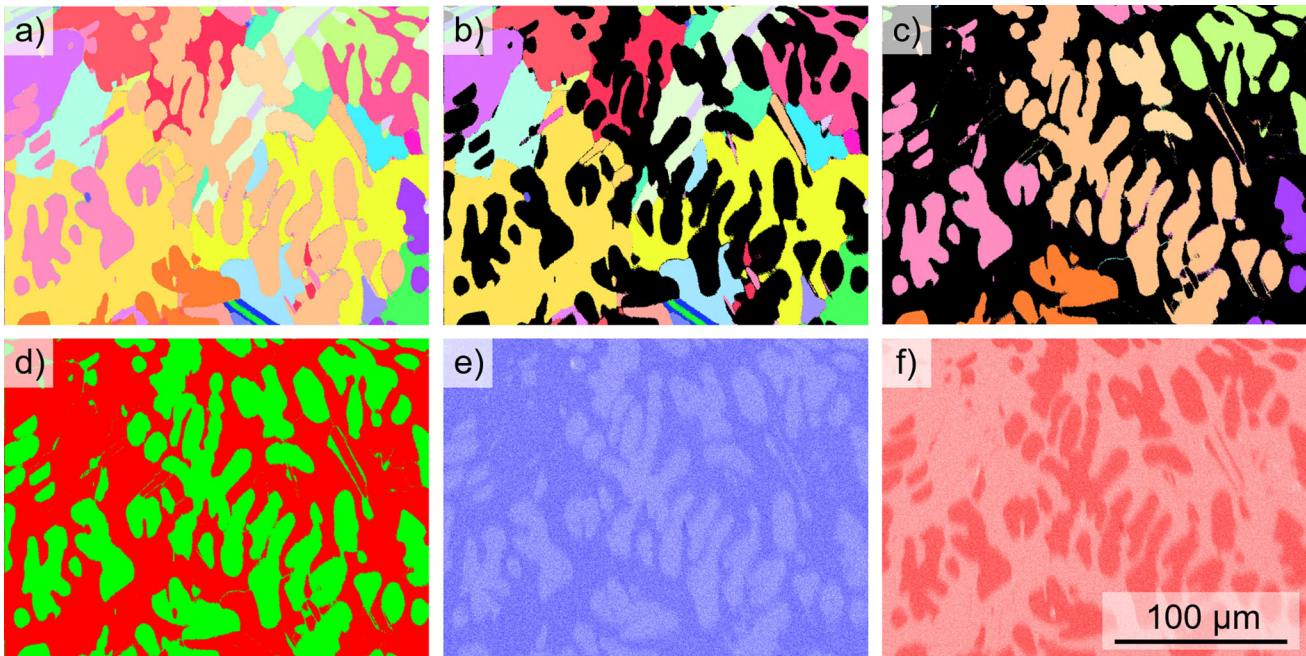
Fig. 11—Combined EBSD and EDS maps of the two-phase region of the binary Laves and μ-phase with a targeted composition of 46 at. pct Ta (sample μ_{b1}); (*a*) IPF of the Laves and μ-phase; (*b*) IPF of only the μ-phase; (*c*) IPF of only the Laves phase; (*d*) color-coded phase map with the μ-phase colored in red and the Laves phase in green; (*e*) EDS map of Ta; (*f*) EDS map of Fe. The scale bar applies to all images (Color figure online).

In addition, for a more detailed characterization of the samples, especially with respect to the presence of second phases, BSE images were taken, which can be seen in Figure 13. The arrangement of the samples of the two TCP phases of the Ta–Fe(–Al) system with different compositions is the same as in the optical micrographs in Figure 12. A detailed discussion of the observed inhomogeneity depending on the targeted composition is given in Section IV–A.

The actual compositions determined by EDS for all samples shown in Figure 13 and the target sample compositions for comparison can be found in Table I.

IV. DISCUSSION

This work aims at the successful synthesis and metallographic preparation of the TCP phases of the Ta–Fe(–Al) system for subsequent investigations regarding their mechanical behavior and deformation mechanisms. The phase diagrams used to plan the sample compositions seem to represent the phase ranges of the Laves and μ-phase well and agree with our observations. However, some pitfalls were encountered during the synthesis, such as incomplete melting of them due to a high amount of Ta and insufficient purity of the input materials. The effect of impurities on solidification and microstructure evolution, *e.g.*, in terms of heterogeneous nucleation in the melt from higher melting particles or a reduction in grain boundary mobility due to solute segregation and Zener drag are well known.[25] Particularly for intermetallics that do not respond well to heat treatment (as was the case here), use of starting

Table III. Reflectors of the Laves and μ-Phase Structures Given with Their hkil Indices

Laves phase	μ-phase
0 0 0 4	0 0 0 1
1 1 $\bar{2}$ 2	1 1 $\bar{2}$ 0
0 2 $\bar{2}$ 1	0 2 $\bar{2}$ 1
2 2 $\bar{4}$ 0	0 2 $\bar{2}$ 4
0 1 $\bar{1}$ 3	0 3 $\bar{3}$ 0
0 3 $\bar{3}$ 0	0 2 $\bar{2}$ $\bar{5}$
0 3 $\bar{3}$ 2	1 1 $\bar{2}$ 6
0 2 $\bar{2}$ 5	0 1 $\bar{1}$ $\overline{10}$
	0 1 $\bar{1}$ 11
	1 2 $\bar{3}$ $\overline{10}$
	1 2 $\bar{3}$ 11

elements with the best possible purity has long been recognized as indispensable[26] and again exemplified in this work. In this context, the type of impurity and, conversely, the list of elements specified in the starting elements chemical analysis appear particularly important, as the elements form highly stable alternative compounds, *e.g.*, TaC with one of the highest known melting points. The detrimental role of C as a non-metallic impurity could not be explicitly quantified here, due to the difficulty in its quantitative measurement by the available EDS method, but is consistent with the much worse results achieved with a Fe starting element of the same given technical purity but without
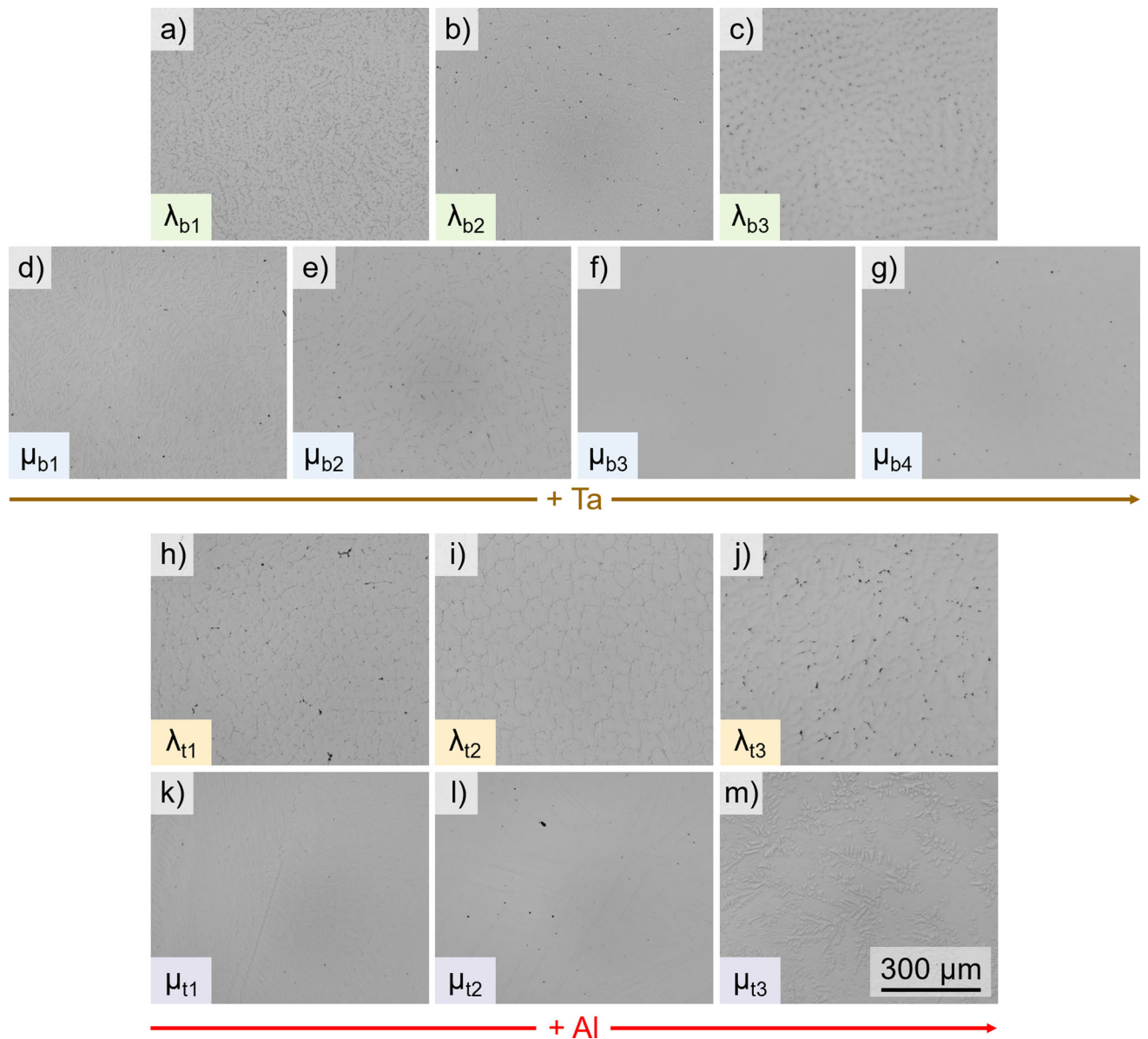
Fig. 12—Optical microscopy images: (a–c) binary Laves phase samples λ_{b1}, λ_{b2}, and λ_{b3} with increasing Ta content of 28, 33, and 38 at. pct; (d–g) binary μ-phase samples μ_{b1}, μ_{b2}, μ_{b3}, and μ_{b4} with increasing Ta content of 46, 50, 54, and 58 at. pct; (h–j) ternary Laves phase samples λ_{t1}, λ_{t2}, and λ_{t3} with 33 at. pct Ta and increasing Al content of 22, 33.5, and 45 at. pct; (k–m) ternary μ-phase samples μ_{t1}, μ_{t2}, and μ_{t3} with 54 at. pct Ta and increasing Al content of 9, 16, and 23 at. pct. All samples contain Fe as the binary or ternary element to balance the alloys to 100 at. pct. The scale bar applies to all images.

quantification of C. Identification and removal of residual surface impurities may be possible in many cases,[26] but in the case of the likely surface oxides on the lower purity Ta, etching of the surface proved insufficient.

In addition to prioritizing high-purity elements, we found that careful planning of the synthesis process is essential,[27] particularly for such difficult systems with in some cases narrow phase ranges as well as very different and partially also very high melting points. The difficulties arising from the strongly differing melting points and the influence of impurities were also addressed for the synthesis of refractory high entropy alloys (RHEAs), whereby possible optimization parameters were identified, but no final evaluation of the significance and impact of the individual parameters was achieved.[28,29] By adjusting the input materials and improving the synthesis route, it was possible to produce the two TCP phases with different stoichiometric and off-stoichiometric compositions. This could also be confirmed after successful metallographic sample preparation by means of microstructural analysis using EDS and EBSD measurements. The analyses showed that the predominantly homogeneous microstructure with sufficient grain size is suitable for nanomechanical testing, which is our immediate application in research of the mechanical properties. But other tests, such as corrosion or electric conductivity testing or *in situ* observations of
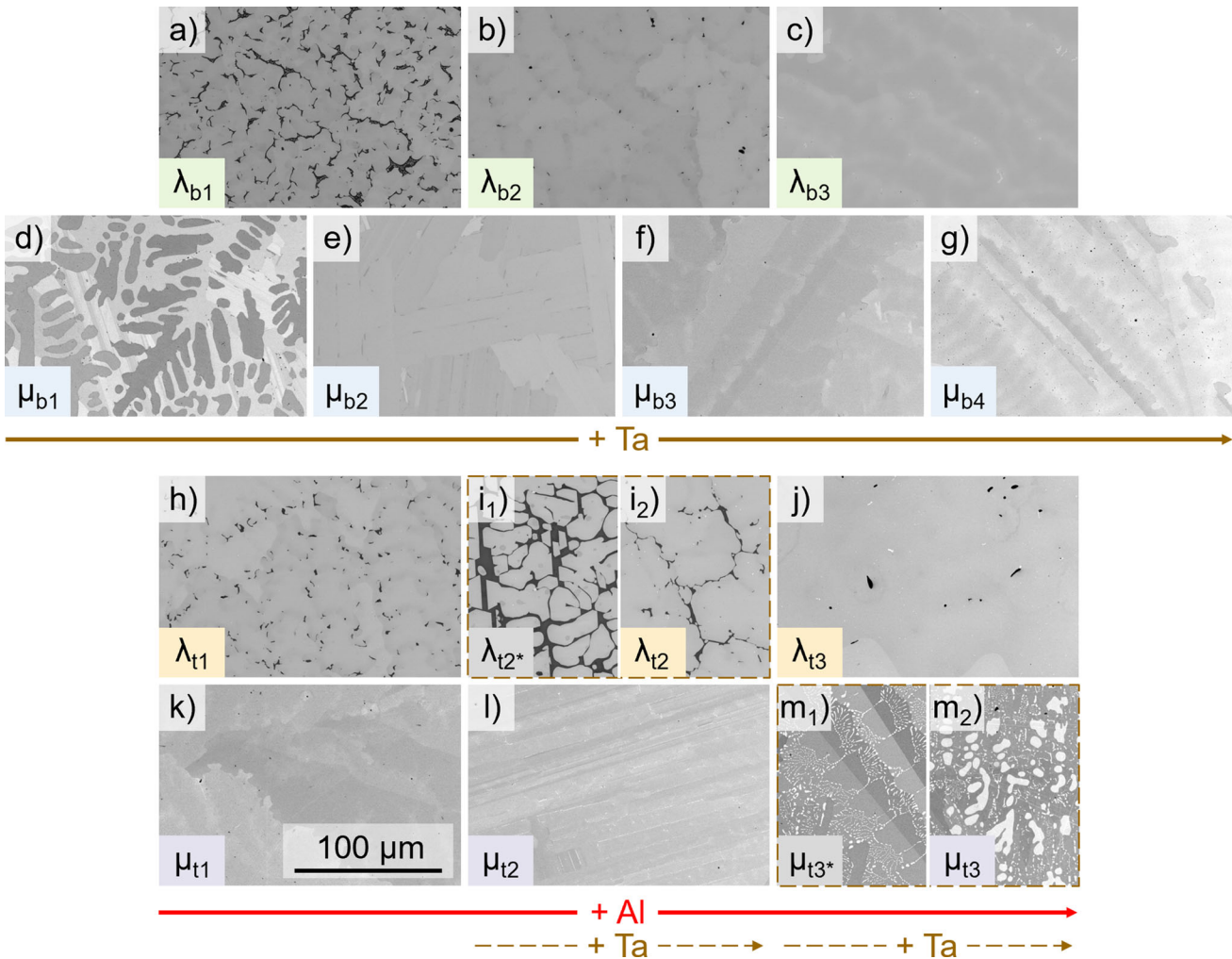
Fig. 13—BSE images: (*a–c*) binary Laves phase samples λ_{b1}, λ_{b2}, and λ_{b3} with increasing Ta content of 28, 33, and 38 at. pct; (*d–g*) binary μ-phase samples μ_{b1}, μ_{b2}, μ_{b3}, and μ_{b4} with increasing Ta content of 46, 50, 54, and 58 at. pct; (*h, i_2* and *j*) ternary Laves phase samples λ_{t1}, λ_{t2}, and λ_{t3} with 33 at. pct Ta and increasing Al content of 22, 33.5, and 45 at. pct; (*k, l* and *m_2*) ternary μ-phase samples μ_{t1}, μ_{t2}, and μ_{t3} with 54 at. pct Ta and increasing Al content of 9, 16, and 23 at. pct. All samples contain Fe as the binary or ternary element to balance the alloys to 100 at. pct. The micrographs for samples λ_{t2*} and μ_{t3*} shown in (i$_1$) and (m$_1$) highlight the effect of a slight reduction in Ta content from 33 to 30 at. pct (with 35 at. pct Fe and Al each) and from 54 to 52 at. pct (with 24 at. pct Fe and Al each), respectively. The scale bar applies to all images.

grain boundary or phase boundary specific properties, *e.g.*, motion or segregation, would also benefit from this size scale.

A. *Remaining Challenges and Limits of Arc Melter Synthesis*

Despite the above-mentioned adjustments and improvements in the sample fabrication, some of the samples still show additional unwanted phases as inhomogeneities. The origin of these and their relation to the underlying phase equilibria and the experimental boundary conditions of arc melting as the core synthesis method will be discussed in the following.

During synthesis inside an arc melter with a water-cooled crucible plate, cooling to below 100 °C happens within a few seconds. In the case studied here, namely an experimental synthesis matrix including the phase boundaries of ternary, high melting phases, this poses

a limit to the phase compositions that can be achieved without the formation of significant volume fractions of a second phase. Where the phase region changes composition as a function of temperature, the synthesis of a homogeneous stoichiometric μ-phase may be impossible and would require an alternative preparation route that can implement very slow cooling particularly at high temperatures.

Samples λ_{b1}, μ_{b1}, λ_{t2} and μ_{t3} present such cases at either end of the phase boundaries with respect to Ta content and a clear second phase visible in Figure 13(a), (d), (i) and (m), respectively. The targeted composition of sample λ_{b1} (Figure 13(a)) is 28 at. pct Ta. According to the Ta–Fe phase diagram (Figure 2 on the left), the phase range of the binary Laves phase begins at 27.7 at. pct Ta and reaches this maximum value at a temperature of 1443 °C. At both higher and lower temperatures, the phase range becomes smaller. The presence of another Fe-rich phase is therefore likely and could indeed be
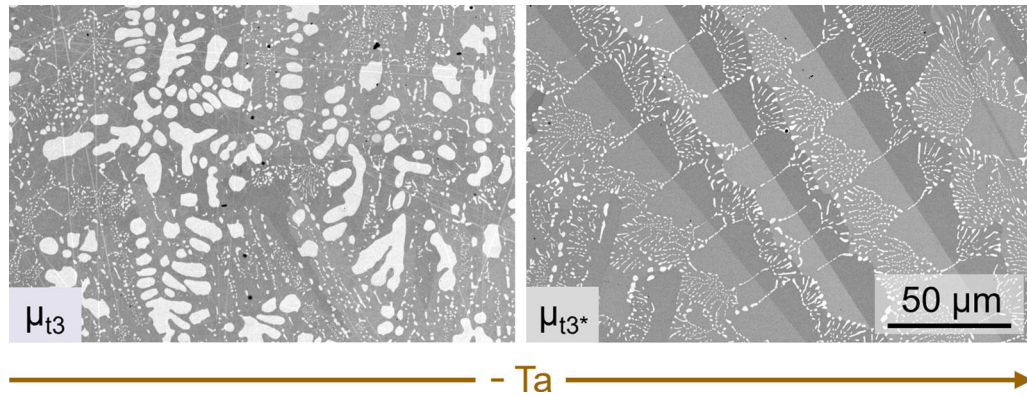
Fig. 14—Reduction of the contained Ta-rich second phase in the ternary μ-phase sample μ_{t3} by reducing the Ta content by 2 at. pct.

confirmed by EDS analysis. Similarly, in the μ-phase sample μ_{b1} with 46 at. pct Ta (closest to the stoichiometric composition of Ta_6Fe_7), the presence of a second phase is likely caused by the two-phase region $(\lambda + \mu)$ present at temperatures above 600 °C. As a result, the phase boundary of the μ-phase is reached only at low temperatures, where diffusion is already limited, impeding a full phase transformation. As expected, a combined EBSD and EDS measurement revealed that the second phase is the Laves phase (cf. Figure 11).

The effect of a slight deviation from the phase region, is clearly visible for the ternary Laves phase. Further reduction of the Ta content in sample λ_{t2} from 33 to 30 at. pct (sample λ_{t2*} with small Ta core), results in an increased formation of the B2 FeAl phase with a dark contrast, as shown in Figure 13(i_1) and (i_2) (and cf. Figure 9). The ternary μ-phase sample μ_{t3} (Figure 13(m)) also has a second phase present which is significantly brighter in the BSE image, indicating that this phase has a higher Ta content. Indeed, decreasing the Ta content from 54 to 52 at. pct Ta at constant Fe:Al ratio leads to a decrease in the proportion of the second phase (sample μ_{t3*}, Figure 14). Again, this composition is close to the phase boundary of the ternary μ-phase, as highlighted in the ternary phase diagram in Figure 2. In this case, the Ta_2Al σ-phase with dissolved Fe could be present. EDS confirms the higher Ta content indicated by the bright BSE contrast, however, the EBSD pattern quality of the precipitates is not sufficient to identify the crystal structure.

As expected, if temperature during solidification cannot be controlled carefully, it is difficult to obtain homogenous sample material close to the boundaries of the phase regions. In some systems, use of more elaborate casting and solidification equipment or employing long heat treatments at the highest possible temperature to encourage retrospective phase transformation may alleviate the problems encountered here. However, in some cases the formation of additional phases may not be avoided entirely even by these measures, particularly where the transformation occurs at temperatures much below the solidus temperature and transformation is sluggish and/or requires substantial compositional changes by diffusion. The Mo–Fe system[30] is an example of such a system, where the R-

and σ-phase form from the melt. The synthesis of samples with a large μ-phase fraction remains reasonably straightforward,[31] with a transformation temperature of 1370 °C, not far from the solidus curve. But the synthesis of bulk Laves phase is in practice largely suppressed at the much lower transformation temperature of 977 °C and after passing two-phase regions involving α-Fe, the R- and μ-phase.[30]

Despite the presence of second phases in samples with compositions close to the boundary of the phase field, a large fraction of the intended phase could be prepared for all cases. The compositions of these phases of interest determined by EDS (last column of Table I), deviate less than 1.5 at. pct from the intended compositions for the majority of the samples. A systematic investigation of the TCP phases of the binary Ta–Fe system with different compositions at increasing Ta content as well as the ternary Ta–Fe–Al system with varying Fe:Al ratio while keeping the Ta content as constant as possible has therefore proven to be achievable.

B. Suitability for Nanomechanical Testing

In spite of these remaining challenges at the phase boundaries, a large matrix of samples could be successfully cast and metallographically prepared for subsequent analysis. Here, we present results of mechanical testing as examples for popular materials testing that require reasonably homogenous but small sample volumes, such as produced by small-scale laboratory arc melting. In the case of brittle materials in particular, macroscopic mechanical testing to unravel plastic deformation mechanisms below the brittle-to-ductile transition temperature is impeded by the prevalence of fracture from small intrinsic flaws. In these cases, nanomechanical testing has been established as the method of choice. Individual nanoindentations can be placed into very small volumes and dimensions down to the depth of a few nanometers reached by indentation using atomic force microscopy or a composite analysis of conventional nanoindentations into thin films. However, where dislocation mechanisms and quantitative material properties are of interest, samples ideally contain a random texture and grain sizes of the order of at least tens of μm. Larger grains enable more
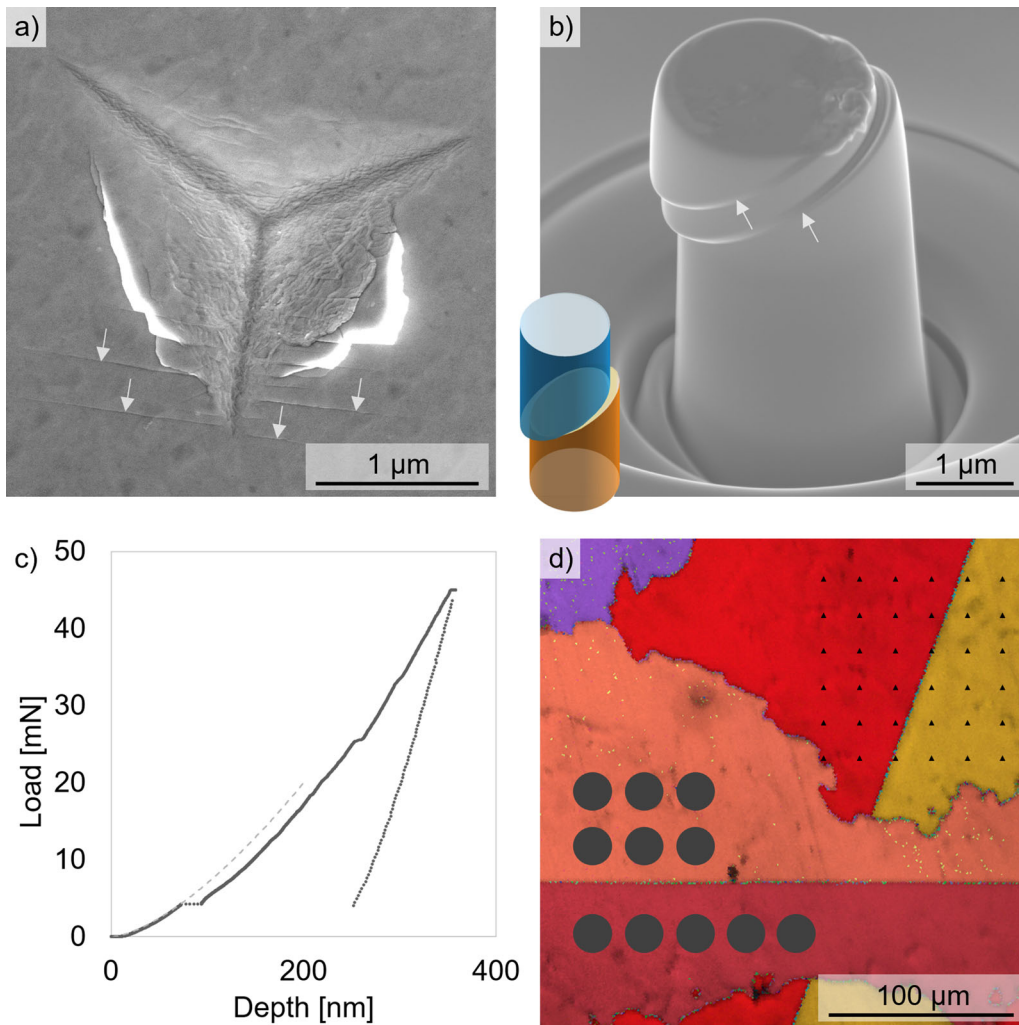
Fig. 15—(a) Indent after nanoindentation with highlighted slip traces; (b) micropillar with marked slip traces and slip plane model in the bottom left corner; (c) typical load-displacement curve from nanoindentation with the fitted elastic curve (Hertz) as dashed line, showing a pronounced pop-in at the elastic-to-plastic transition and subsequent serrated yielding; (d) typical EBSD map (IPF + IQ) with drawn symbols for micropillars (circles) and an indent array (triangles), to show the ratio between the grain size and the performed experiments.

in-depth analyses, such as a statistical determination of the relative activity of different slip planes or milling and testing of several micropillar compression samples. As an indirect requirement emerges a very high surface flatness and quality with few mechanically induced defects. These result from the small volumes interrogated in nanomechanical testing and the need for good EBSD pattern to allow the usually intended correlation between crystal orientation and deformation.

The synthesis and metallographic preparation methods presented in this work now make this kind of research possible for the Ta–Fe(–Al) system. To illustrate this, both nanoindentation and microcompression data are presented (Figure 15) in addition to the EBSD data already introduced above.

Figure 15 shows typical electron micrographs of a nanoindentation imprint in image (a), a deformed microcompression sample in (b), a nanoindentation load-displacement curve in (c) and an EBSD map on which a typical indentation array and locations for microcompression are indicated schematically in (d). In both

micrographs, slip traces around the indent and on the micropillar, marked with small arrows, are clearly visible and the possible activated slip systems can be determined based on the local crystal orientation.[32] The dominant formation of slip traces around the indentation on only one set of parallel planes confirms the prevalence of basal slip in the μ-phase, consistent with observations by Luo et al.[19,33] on Nb–Co μ-phases with similar compositions in terms of the ratio of A and B atoms.

In addition to the characterization of mechanical properties and mechanisms, nanoindentation can also serve as a probe for the defect density at the surface after metallographic preparation. Where the stress field directly underneath the indenter samples a defect free volume, plastic deformation can only begin upon nucleation of dislocations. As dislocation nucleation requires higher stress than dislocation multiplication and motion, although the difference is much smaller in hard intermetallics than in soft metals, a so-called 'pop-in' occurs as the sample is loaded. Where this sudden displacement jump occurs at a stress level of the

order of the theoretical shear strength of the material, it has been shown to be associated with dislocation nucleation in an originally defect free volume. Such a pop-in is indeed observed here in most indentation load-displacement curves, as indicated in Figure 15(c). The diamond indentation tip is of Berkovich shape overall (cf. Figure 15(a)) but is not infinitely sharp at its very end. At this point, it can normally be approximated by a sphere, giving rise to the elastic, Hertzian contact at the start of the indentation. A fit to the curve assuming a fully elastic Hertzian contact (Figure 15(c)) then allows an estimate of the maximum shear stress under the indenter, that is the point where dislocation nucleation is thought to take place and from where dislocations move very rapidly outwards to cause the displacement jump observed in the load-displacement signal. Here, the Youngs modulus of the sample is taken as 290 GPa, approximated from the indentation modulus, the Poisson ratio is assumed as 0.32, the tip radius as 275 nm and the surface as flat (sphere radius $=$ infinity). These values provide a good fit to the data and at the load corresponding to the pop-in, the maximum shear stress in the volume under Hertzian contact conditions is 27 GPa.[34] This is even slightly higher than the approximated ideal shear strength taken as $\tau_{\text{theo}} = \frac{G}{2\pi}$, resulting in 17.5 GPa. The shear modulus G is thereby estimated to be $G = \frac{E}{2(1+v)}$, based on the Youngs modulus E and Poisson ratio v, as used above. The deviation between the maximum shear stress and ideal shear strength values is very likely due to the approximate values used to fit the data as well as the assumptions of perfect Hertzian contact and isotropic behavior of the TCP phase both in terms of elasticity and availability of a suitable slip system with the maximum shear stress resolved on it. Overall, the pop-in is therefore taken as an indication of dislocation nucleation and thereby provides another source of evidence for the successful surface preparation in addition to the high-quality EBSD patterns acquired on the samples (cf. Figure 10).

V. CONCLUSIONS

We presented possible routes for the synthesis of the Laves and μ-phases of the Ta–Fe(–Al) system by arc melting and characterized the resulting samples for subsequent property analysis both chemically and structurally. In particular, we recommend points to consider for a successful analysis of binary and ternary TCP phases in terms of starting materials, the order and stepwise manner of element addition and dealing with the inherent brittleness of these intermetallics.

Our main conclusions are

- Input materials with a very high degree of purity are indispensable for homogeneous samples.
- The scope for improving the microstructure in terms of homogeneity of the phases and grain size by subsequent heat treatment is very limited, at least for the temperature range tested using commonly available furnaces in a research context.
- Consequently, during synthesis of ternary TCP phases, the phase range should not be left. This can be achieved by stepwise melting and addition of suitable fractions of the overall elements to form the final ternary phase.
- Preparation of both binary and ternary phases in the Ta–Fe(–Al) system with suitable grain size and homogeneity as well as a low surface dislocation density for subsequent microstructural and nanomechanical analysis is possible by careful synthesis in a small-scale laboratory arc melter.
- Limits to the methods are encountered near the phase boundaries, where avoidance of the adjacent two-phase regions becomes exceedingly difficult. For such samples, controlled cooling has been identified as an additional requirement.

The presented synthesis and preparation routes and most important pitfalls and opportunities for improvement of synthesis conditions are based on the binary Ta–Fe and ternary Ta–Fe–Al systems. We expect that most aspects can be transferred also to other systems with intermetallic phases, particularly where their stability range extends from the solidus line to room temperature. The purpose of this work was therefore also to assist the study of other comparable transition metal intermetallic phases. We hope that in this way, these complex crystals will be much better understood in the future and that the type of samples made available in this work will also be of benefit to the increasingly microscopic studies of other properties and mechanisms, e.g., in electrochemistry,[35] electrical conductivity,[36] or interaction with hydrogen,[37] in addition to plastic deformation under mechanical load.

OPEN ACCESS

DATA AVAILABILITY

Data will be made available on request.

COMPETING INTERESTS

On behalf of all authors, the corresponding author states that there is no conflict of interest.

SUPPLEMENTARY INFORMATION

The online version contains supplementary material available at https://doi.org/10.1007/s11661-024-07390-z.

REFERENCES

1. G. Sauthoff: *Intermetallics*, Wiley-VCH, Weinheim, 1995.
2. J.D. Livingston: *Phys. Status Solidi A*, 1992, vol. 131(2), pp. 415–23. https://doi.org/10.1002/pssa.2211310215.
3. U. Krämer and G.E.R. Schulze: *Krist. Tech.*, 1968, vol. 3(3), pp. 417–30. https://doi.org/10.1002/crat.19680030308.
4. A.K. Sinha: *Prog. Mater. Sci.*, 1972, vol. 15(2), pp. 81–185. https://doi.org/10.1016/0079-6425(72)90002-3.
5. S. Andersson: *J. Solid State Chem.*, 1978, vol. 23(1–2), pp. 191–204. https://doi.org/10.1016/0022-4596(78)90065-8.
6. S. Korte-Kerzel: *MRS Commun.*, 2017, vol. 7(2), pp. 109–20. https://doi.org/10.1557/mrc.2017.15.
7. H. Okamoto: *J. Phase Equilib. Diffus.*, 2013, vol. 34(2), pp. 165–66. https://doi.org/10.1007/s11669-012-0164-3.
8. V. Raghavan: *J. Phase Equilib. Diffus.*, 2013, vol. 34(4), pp. 328–49. https://doi.org/10.1007/s11669-013-0239-9.
9. V.T. Witusiewicz, A.A. Bondar, U. Hecht, V.M. Voblikov, N.I. Tsyganenko, O.S. Fomichov, M.V. Karpets, V.M. Petyukh, and T.Y. Velikanova: *J. Mater. Sci.*, 2013, vol. 48(1), pp. 377–412. https://doi.org/10.1007/s10853-012-6755-x.
10. E. Ganglberger, H. Nowotny, and F. Benesovsky: *Monatsh. Chem.*, 1965, vol. 96(5), pp. 1658–59. https://doi.org/10.1007/BF00902104.
11. L. Pauling: *J. Am. Chem. Soc.*, 1947, vol. 69(3), pp. 542–53. https://doi.org/10.1021/ja01195a024.
12. N.N. Greenwood and A. Earnshaw: *Chemistry of the Elements*, 2nd ed. Elsevier-Butterworth-Heinemann, Amsterdam, 2010.
13. H. Sicius: *Erdmetalle: Elemente der dritten Hauptgruppe*, 1st ed. Springer Fachmedien Wiesbaden, Wiesbaden, 2016.
14. Ž. Blažina and S. Pavković: *J. Less-Common Met.*, 1989, vol. 155(2), pp. 247–53. https://doi.org/10.1016/0022-5088(89)90234-8.
15. C.G. Wilson, D.K. Thomas, and F.J. Spooner: *Acta Crystallogr.*, 1960, vol. 13(1), pp. 56–57. https://doi.org/10.1107/S0365110X60000121.
16. A. Raman: *Trans. Indian Inst. Met.*, 1966, vol. 19, pp. 202–05.
17. A. Raman: *Z. Metallkd.*, 1966, vol. 57, pp. 301–05.
18. X. Wu, W. Liu, X.-G. Lu, Y. Jiang, and Y. He: *J. Solid State Chem.*, 2022, vol. 305, p. 122704. https://doi.org/10.1016/j.jssc.2021.122704.
19. W. Luo, Z. Xie, S. Zhang, J. Guénolé, P.-L. Sun, A. Meingast, A. Alhassan, X. Zhou, F. Stein, L. Pizzagalli, B. Berkels, C. Scheu, and S. Korte-Kerzel: *Adv. Mater.*, 2023, vol. 35(24), p. 2300586. https://doi.org/10.1002/adma.202300586.
20. C.R. Hunt and A. Raman: *Int. J. Mater. Res.*, 1968, vol. 59(9), pp. 701–07. https://doi.org/10.1515/ijmr-1968-590903.
21. K. Momma and F. Izumi: *J. Appl. Crystallogr.*, 2008, vol. 41(3), pp. 653–58. https://doi.org/10.1107/S0021889808012016.
22. V.T. Witusiewicz, A.A. Bondar, U. Hecht, V.M. Voblikov, O.S. Fomichov, V.M. Petyukh, and S. Rex: *Intermetallics*, 2011, vol. 19(7), pp. 1059–75. https://doi.org/10.1016/j.intermet.2011.03.018.
23. W.C. Oliver and G.M. Pharr: *J. Mater. Res.*, 1992, vol. 7(6), pp. 1564–83. https://doi.org/10.1557/JMR.1992.1564.
24. W.C. Oliver and G.M. Pharr: *J. Mater. Res.*, 2004, vol. 19(1), pp. 3–20. https://doi.org/10.1557/jmr.2004.19.1.3.
25. G. Gottstein: *Materialwissenschaft und Werkstofftechnik*, 4th ed. Springer, Berlin, 2014.
26. R. Pöttgen and D. Johrendt: *Intermetallics*, 2nd ed. De Gruyter, Berlin, 2019.
27. H. Schäfer: *Angew. Chem.*, 1971, vol. 83(1), pp. 35–42. https://doi.org/10.1002/ange.19710830105.
28. O.N. Senkov, D.B. Miracle, K.J. Chaput, and J.-P. Couzinie: *J. Mater. Res.*, 2018, vol. 33(19), pp. 3092–128. https://doi.org/10.1557/jmr.2018.153.
29. Y. Gao, K. Chong, L. Qiao, Y. Li, C. Liu, F. Guo, D. Wu, and Y. Zou: *Mater. Des.*, 2023, vol. 228, p. 111820. https://doi.org/10.1016/j.matdes.2023.111820.
30. A.F. Guillermet: *Bull. Alloy Phase Diagrams*, 1982, vol. 3(3), pp. 359–67. https://doi.org/10.1007/BF02869315.
31. S. Schröders, S. Sandlöbes, C. Birke, M. Loeck, L. Peters, C. Tromas, and S. Korte-Kerzel: *Int. J. Plast.*, 2018, vol. 108, pp. 125–43. https://doi.org/10.1016/j.ijplas.2018.05.002.
32. J.S.K.-L. Gibson, R. Pei, M. Heller, S. Medghalchi, W. Luo, and S. Korte-Kerzel: *Materials*, 2021, vol. 14(2), p. 407. https://doi.org/10.3390/ma14020407.
33. W. Luo, Z. Xie, P.-L. Sun, J.S.K.-L. Gibson, and S. Korte-Kerzel: *Acta Mater.*, 2023, vol. 246, p. 118720. https://doi.org/10.1016/j.actamat.2023.118720.
34. K.L. Johnson: *Contact Mechanics*, Cambridge University Press, Cambridge, 1985.
35. C. Luan, J. Angona, A. Bala Krishnan, M. Corva, P. Hosseini, M. Heidelmann, U. Hagemann, E. Batsa Tetteh, W. Schuhmann, K. Tschulik, and T. Li: *Angew Chem.*, 2023, vol. 62(28), p. e202305982. https://doi.org/10.1002/anie.202305982.
36. T. Kaiser, G. Dehm, C. Kirchlechner, A. Menzel, and H. Bishara: *Eur. J. Mech. A Solids*, 2023, vol. 97, p. 104777. https://doi.org/10.1016/j.euromechsol.2022.104777.
37. J. Rao, S. Lee, G. Dehm, and M.J. Duarte: *Mater. Des.*, 2023, vol. 232, p. 112143. https://doi.org/10.1016/j.matdes.2023.112143.